

DTIC FILE COPY

4

GL-TR-89-0239

AD-A216 329

Super-Micro Computer Weather Prediction Model

Keith L. Seitter and Frank P. Colby, Jr.

University of Lowell
Department of Earth Sciences
One University Avenue
Lowell, MA 01854

August 1989

Scientific Report No. 1

Approved for public release; distribution unlimited

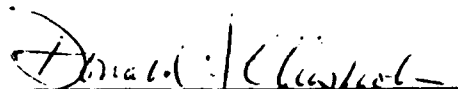
GEOPHYSICS LABORATORY
AIR FORCE SYSTEMS COMMAND
UNITED STATES AIR FORCE
HANSCom AIR FORCE BASE, MASSACHUSETTS 01731-5000

DTIC
ELECTE
JAN 02 1990
S B D


90 01 02 055

"This technical report has been reviewed and is approved for publication"


H. STUART MUENCH
Contract Manager


DONALD A. CHISHOLM, Chief
Atmospheric Prediction Branch

FOR THE COMMANDER


ROBERT A. McCLATCHEY, Director
Atmospheric Sciences Division

This document has been reviewed by the ESD Public Affairs Office (PA) and is releasable to the National Technical Information Service (NTIS).

Qualified requestors may obtain additional copies from the Defense Technical Information Center. All others should apply to the National Technical Information Service.

If your address has changed, or if you wish to be removed from the mailing list, or if the addressee is no longer employed by your organization, please notify AFGL/DAA, Hanscom AFB MA 01731-5000. This will assist us in maintaining a current mailing list.

Do not return copies of this report unless contractual obligations or notices on a specific document requires that it be returned.

REPORT DOCUMENTATION PAGE				Form Approved OMB No. 0704-0188	
1a. REPORT SECURITY CLASSIFICATION Unclassified			1b. RESTRICTIVE MARKINGS		
2a. SECURITY CLASSIFICATION AUTHORITY			3. DISTRIBUTION / AVAILABILITY OF REPORT Approved for public release; Distribution unlimited		
2b. DECLASSIFICATION / DOWNGRADING SCHEDULE			4. PERFORMING ORGANIZATION REPORT NUMBER(S)		
6a. NAME OF PERFORMING ORGANIZATION University of Lowell			6b. OFFICE SYMBOL (If applicable)		
6c. ADDRESS (City, State, and ZIP Code) Department of Earth Sciences One University Avenue Lowell, MA 01854			7a. NAME OF MONITORING ORGANIZATION Geophysics Laboratory		
8a. NAME OF FUNDING / SPONSORING ORGANIZATION			8b. OFFICE SYMBOL (If applicable)		
8c. ADDRESS (City, State, and ZIP Code)			9. PROCUREMENT INSTRUMENT IDENTIFICATION NUMBER F19628-88-K-0016		
			10. SOURCE OF FUNDING NUMBERS		
			PROGRAM ELEMENT NO. 61102F	PROJECT NO. ILIR	TASK NO. 8K
			WORK UNIT ACCESSION NO. AA		
11. TITLE (Include Security Classification) Super-Micro Computer Weather Prediction Model					
12. PERSONAL AUTHOR(S) Keith L. Seitter and Frank P. Colby, Jr.					
13a. TYPE OF REPORT Scientific #1		13b. TIME COVERED FROM _____ TO _____		14. DATE OF REPORT (Year, Month, Day) 1989 August	
15. PAGE COUNT 42					
16. SUPPLEMENTARY NOTATION					
17. COSATI CODES			18. SUBJECT TERMS (Continue on reverse if necessary and identify by block number)		
FIELD	GROUP	SUB-GROUP	Mesoscale Modeling Weather Forecasting		
			Computer Simulation Models		
			Boundary Layer Parameterizations		
19. ABSTRACT (Continue on reverse if necessary and identify by block number)					
<p>A meso-beta scale model is being developed to provide forecast guidance in the 3 to 18 hour time period. The model is intended for use at local base weather offices equipped with a super-micro class computer, allowing these offices to produce local forecast guidance for their region.</p> <p>The model consists of a four-layer sigma-coordinate model which has a two-layer boundary layer model nested within its lowest layer. The vertically nested two-layer model allows direct calculation of boundary layer quantities through simple parameterizations for radiative processes and surface fluxes. The model has a 480 x 480 km horizontal domain with 20 km resolution which is nested horizontally, using a two-way interactive procedure, within a 1320 x 1320 km coarse grid domain with 60 km resolution.</p> <p>This report presents the equation sets for the nested model and the physical parameterizations. It also summarizes tests of the nested four-layer/two-layer model structure which have been completed, and separate tests of the parameterization package.</p>					
20. DISTRIBUTION / AVAILABILITY OF ABSTRACT <input type="checkbox"/> UNCLASSIFIED/UNLIMITED <input type="checkbox"/> SAME AS RPT. <input type="checkbox"/> DTIC USERS			21. ABSTRACT SECURITY CLASSIFICATION Unclassified		
22a. NAME OF RESPONSIBLE INDIVIDUAL H. Stuart Muench			22b. TELEPHONE (Include Area Code)		22c. OFFICE SYMBOL GL/LYP

Table of Contents

1. Introduction	1
2. Model Description	
a. Basic model equations	2
b. Vertical and horizontal nesting in the model	5
c. Other numerical details	9
3. Tests with the Model	
a. Tests with VTWIN	11
b. Tests with the HVN model	18
4. Boundary Layer Parameterization	
a. Radiation	21
b. Surface energy balance	24
c. Ground variables	27
d. Boundary layer height	30
e. Boundary layer variables	33
5. Conclusions and Future Work	34
References	36



Accession For	
NTIS GRA&I	<input checked="checked" type="checkbox"/>
DTIC TAB	<input type="checkbox"/>
Unannounced	<input type="checkbox"/>
Justification _____	
By _____	
Distribution/ _____	
Availability Codes	
Dist	Avail and/or Special
A-1	

1. Introduction

Trajectory and advection models (Muench 1983; Muench and Chisholm 1985; Muench 1989) and automated display systems such as McIDAS and PROFS (Schlatter et al. 1985) show promise of providing added guidance for the very short term forecasting range of 0 to 6 hours. Full synoptic models such as the LFM and NGM have skill from about 12 hours to beyond 48 hours. However, both of these approaches fall short in the 6 to 18 hour period which is perhaps the most vital to the terminal forecaster. It is in this period that meso- β scale disturbances (such as fronts or squall lines) which are in the local area will have an immediate impact on the terminal forecast. Advection models begin failing after a few hours because of synoptic and mesoscale changes in wind patterns and because topographic and geographic influences are often not incorporated (Muench 1983; Muench 1989). On the other hand, the initialization of synoptic scale models is based on synoptic scale data which does not normally include mesoscale features present at the time of initialization. Hence, the synoptic scale model cannot be expected to forecast these mesoscale features.

Several research mesoscale models exist which are capable of providing forecasts on the desired space and time scales (see Pielke 1984, Appendix B, for a partial list of current research mesoscale models). However, these models tend to be just as computationally intensive as operational synoptic scale models, which limits their practicability in an operational setting — each region of the country would require a dedicated supercomputer to provide mesoscale guidance for that region. The research reported here seeks to provide regional mesoscale guidance using a different approach which is well-suited for an operational setting. A meso- β model is being developed which is capable of providing an operationally useful forecast on a super-micro computer (Vax 3 class). Such a model could then be run "in-house" at each forecast office to provide guidance for a region centered on that office. This approach requires the formulation of a model which is considerably different from current research mesoscale models. The goal is to develop a model which has many fewer levels and less complicated physical parameterizations than

research models, but which is still capable of reproducing the physical processes important to mesoscale systems.

The next section will describe the mathematical formulation of the model being developed here including the numerical treatment and physical parameterizations. Section 3 will present results of tests which have been conducted with various prototype versions of the model. The radiation and boundary layer parameterizations, which are crucial to the unique aspects of the model being developed, are described in some detail in section 4. Section 5 gives our conclusions at the end of the first year of model development and outlines the research which will be continuing in the future.

2. Model Description

a. Basic Model Equations

Mesoscale models capable of simulating atmospheric phenomena have existed for more than a decade (Anthes and Warner 1978; Nickerson 1979), and the equation set in σ -coordinates [$\sigma = (p - p_t) / (p_s - p_t)$ where p_s is the surface pressure and p_t is a pressure level specified as the top of the model (we take $p_t = 100$ mb for this study)] is well established. As discussed above, however, these models would require a supercomputer environment in order to run operationally. To develop a mesoscale model which can run operationally on a relatively small computer, we must take a substantially different approach.

The two obvious ways in which to increase the speed of a three-dimensional model -- reducing the number of layers or decreasing the domain size -- are clearly inadequate in and of themselves. The first, by itself, would lead to inadequate treatment of processes near the surface because the boundary layer would no longer be resolved. The second would decrease the predictive time for any mesoscale phenomena not produced by local forcing since it is impossible for mesoscale disturbances to advect into the domain. We do seek to decrease the number of model layers in order to decrease the number of computations per time step, but we avoid problems near the surface by treating the boundary layer explicitly.

Much of the local forcing for mesoscale processes takes place in the planetary boundary layer. Previous mesoscale models packed many layers near the surface to resolve boundary-layer thickness and to adequately calculate fluxes there (see, for example, the ν -coordinate model of Nickerson 1979). We have developed a two-layer model whose lowest layer represents the boundary layer. This layer is not fixed in pressure or σ and is allowed to *change its depth as function of time* — representing the physical structure of the variable depth boundary layer. The fluxes from the surface into this layer as well as the fluxes from the boundary layer into the layer above are calculated directly. A new concept here is the two-way interactive nesting of this two-layer model into the lowest layer of a four-layer σ -coordinate model.

The equation set for the four-layer model is essentially identical to that of Anthes and Warner (1978). The map factor has not been included in our set because a scale analysis indicates this term is not significant for the meso- β scale domains we will be considering. The lowest layer of the four-layer model is on the order of 200 mb thick. It is defined by the surface ($\sigma=1$) and the constant σ surface at $\sigma=\sigma_h$ (see Fig. 1). The two-layer model is nested within this layer, with the σ_h surface which divides the two-layer model representing the variable depth of the planetary boundary layer as a function of x , y , and t . Since σ_h is variable in sigma, computations in the two-layer model require a coordinate transformation into a system in which σ_h represents a constant coordinate surface. We call this new coordinate system "boundary layer coordinates" and denote it with the variable η . We define η as

$$\eta = \frac{\sigma - \sigma_h}{H} \quad H = \begin{cases} \sigma_h - \sigma_{h,0} & \sigma < \sigma_h \\ 1 - \sigma_h & \sigma > \sigma_h \end{cases} \quad (2.1)$$

Prognostic equations for u and v momentum, π ($=p_s - p_r$), and temperature, as well as diagnostic equations for vertical velocity in the η system and the hydrostatic relation become:

$$\begin{aligned} \frac{\partial \pi H u}{\partial t} + \frac{\partial u \pi H u}{\partial x} + \frac{\partial v \pi H u}{\partial y} + \frac{\partial (\eta \pi H u)}{\partial \eta} + \pi H \frac{\partial \phi}{\partial x} \\ = \frac{\pi H R T}{(\pi H \eta + \pi \sigma_h + p_r)} \left[\eta \frac{\partial H}{\partial x} + \frac{\partial \sigma_h}{\partial x} + \eta H + \sigma_h \frac{\partial \pi}{\partial x} \right] + f \pi H v + \pi H F_u \end{aligned} \quad (2.2)$$

$$\begin{aligned} \frac{\partial \pi H v}{\partial t} + \frac{\partial u \pi H v}{\partial x} + \frac{\partial v \pi H v}{\partial y} + \frac{\partial}{\partial \eta} (\eta \pi H v) = - \pi H \frac{\partial \phi}{\partial y} \\ - \frac{\pi H R T}{(\pi H \eta + \pi \sigma_h + p_r)} \left[\eta \frac{\partial H}{\partial y} + \frac{\partial \sigma_h}{\partial y} + (\eta H + \sigma_h) \frac{\partial \pi}{\partial y} \right] + f \pi H u + \pi H F_v \end{aligned} \quad (2.3)$$

$$\begin{aligned} \frac{\partial \pi}{\partial t} = - \int_{-1}^{\sigma_{k+1}} \left[\frac{\partial \pi u}{\partial x} + \frac{\partial \pi v}{\partial y} \right] d\sigma - \int_{-1}^0 \left[\frac{\partial}{\partial x} (H_1 \pi u) + \frac{\partial}{\partial y} (H_1 \pi v) \right] d\eta \\ - \int_0^1 \left[\frac{\partial}{\partial x} (H_2 \pi u) + \frac{\partial}{\partial y} (H_2 \pi v) \right] d\eta \end{aligned} \quad (2.4)$$

$$\begin{aligned} \frac{\partial \pi H T}{\partial t} + \frac{\partial u \pi H T}{\partial x} + \frac{\partial v \pi H T}{\partial y} + \frac{\partial}{\partial \eta} (\eta \pi H T) = \\ - \frac{H R T \omega}{c_p (\pi H \eta + \pi \sigma_h + p_r - \pi_r)} - \frac{\pi H Q}{c_p} + \pi H F_T \end{aligned} \quad (2.5)$$

$$\begin{aligned} 2(H\eta)_{\eta=0} = \frac{1}{\pi} H_2 - H_1 \frac{\partial \pi}{\partial t} - \int_{-1}^0 \left[\frac{\partial}{\partial x} (H_1 \pi u) + \frac{\partial}{\partial y} (H_1 \pi v) \right] d\eta \\ - \int_0^1 \left[\frac{\partial}{\partial x} (H_2 \pi u) + \frac{\partial}{\partial y} (H_2 \pi v) \right] d\eta + \sigma_{k+1} \end{aligned} \quad (2.6)$$

$$\frac{\partial \phi}{\partial \ln (\pi H + \sigma_h + p_r - \pi_r)} = - R T \quad (2.7)$$

where

η = vertical velocity in η -coordinates

ω = pressure vertical velocity (dp/dt)

σ_{k+1} = vertical velocity at the σ_{k+1} interface

ϕ = geopotential

F = friction term

R = specific gas constant for dry air

c_p = specific heat of dry air at constant pressure

f = Coriolis parameter.

In (2.4) and (2.6), H_1 and H_2 refer to the values of H in the upper and lower layers of the two-layer model, respectively [see (2.1)].

The pressure vertical velocity, ω , is found through a diagnostic relation for each η layer

$$\begin{aligned} \omega = (\eta H + \sigma_h) & \left[\frac{\partial \pi}{\partial t} + u \frac{\partial \pi}{\partial x} + v \frac{\partial \pi}{\partial y} \right] \\ & + (\eta \pm 1) \left[\frac{\partial \sigma_h}{\partial t} + u \frac{\partial \sigma_h}{\partial x} + v \frac{\partial \sigma_h}{\partial y} \right] + \pi \eta H \end{aligned} \quad (2.8)$$

where the $+$ or $-$ sign in the second term on the RHS is chosen for the upper and lower layers, respectively. Note that this expression includes explicitly the temporal and spatial variation of the boundary layer height, σ_h . The boundary layer height is a product of the boundary layer parameterization (see section 4), and the rate of change of this height ($\partial \sigma_h / \partial t$) is also computed in the parameterization scheme for use in (2.8).

While σ -coordinate prognostic variables are weighted by π in the typical formulation (see Anthes and Warner 1978), it is obvious in the above equations that η -coordinate variables are weighted by πH . Other prognostic equations similar to (2.5) can be written to provide tendencies for trace variables such as specific humidity.

b. Vertical and horizontal nesting in the model

The merger of the two-layer model into the four-layer model represents a classical two-way interactive nesting problem. The two-layer model actually replaces the lowest layer of the four-layer model. Information from the upper three layers of the four-layer model is passed to the two-layer model through vertical differences across the interface separating the models as well as through the downward integration of divergence in the calculation of change in surface pressure [the first term on the RHS of (2.4)]. The four-layer model also provides $\sigma_{b,m}$ for use in (2.6). Information is passed back from the two-layer to the four-layer model through vertical differences across the interface and through the π -weighting of variables in the four-layer σ -coordinate model (since π includes contributions from all layers). Even though no prognostic equations are solved in

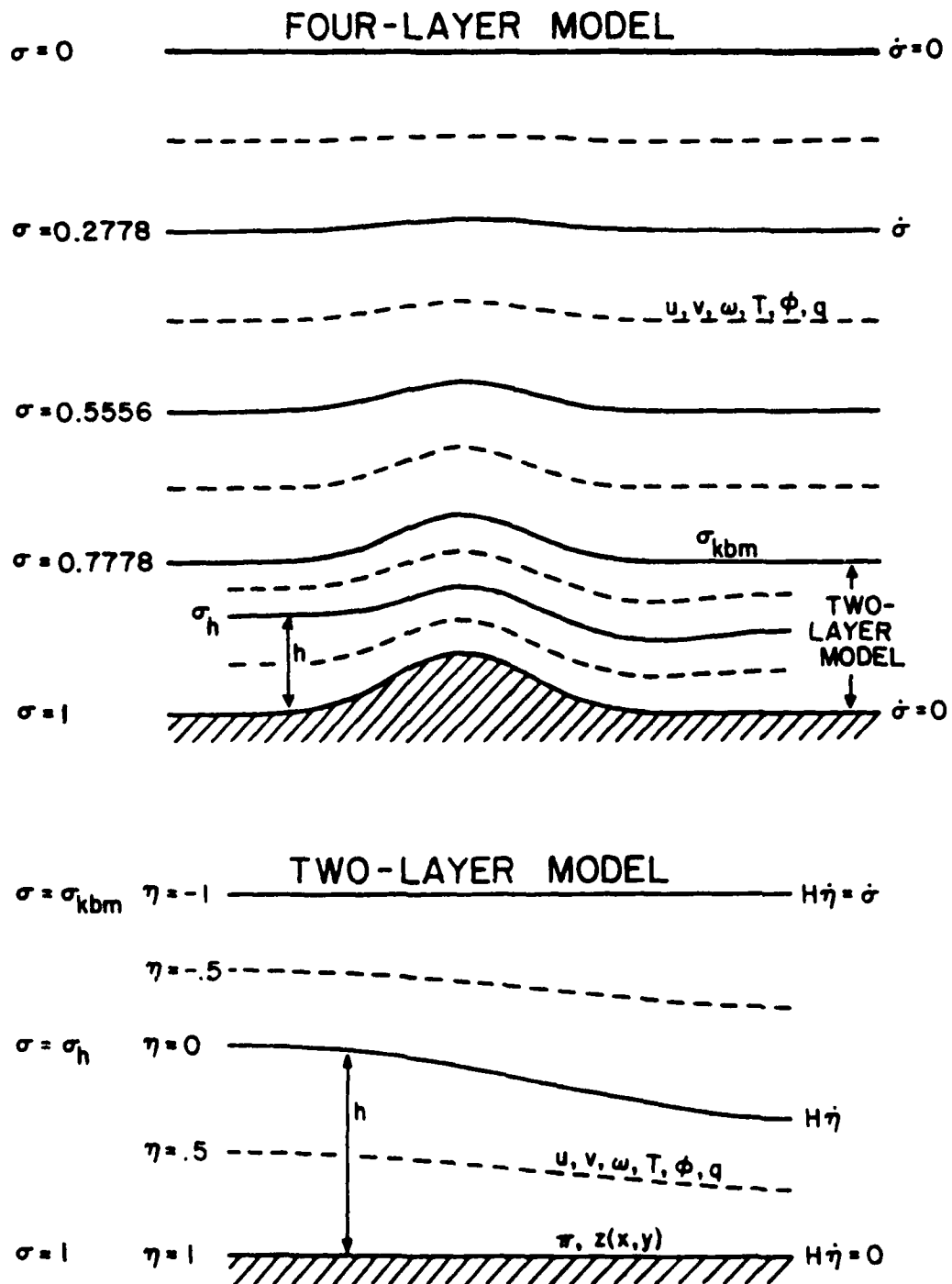


FIG. 1. Schematic structure of the four-layer and two-layer models.

the lowest layer of the four-layer model, values of the variables appropriate for this sigma level are formed by *H*-weighted vertical averages of the two-layer model values. These averaged values are the ones used in the vertical differencing of the four-layer model and represent the means of feedback from the two-layer to the four-layer model.

A staggered grid is used in both the vertical and horizontal directions. In the vertical, all variables are layer quantities except vertical velocities, which are defined at interface levels (see Fig. 1). Horizontally, velocities are defined on staggered points ("x" points in Fig. 2) which surround the points on which all other variables are defined ("o" points in Fig. 2). In order to increase the overall model domain size and move the lateral boundaries away from the area of primary interest, a horizontal nesting of the model is employed as developed by Zhang et al. (1986). The horizontal gridpoint structure of the nested model domains is shown in Fig. 2. A fine grid mesh (FGM) with 20 km resolution is nested in a coarse grid mesh (CGM) with 60 km resolution. A 3:1 ratio of FGM points to CGM points is necessary with a staggered grid so that both "x" and "o" points can be coincident in the overlap region (Zhang et al. 1986). The CGM domain covers 1320 km x 1320 km while the FGM domain is 480 km x 480 km for "o" points (all displays will be made on "o" point arrays, with any displayed velocities being averaged to these points). The two-way interactive nesting procedure of Zhang et al. (1986) is used with a few minor modifications. First, in the calculation of tendencies for the "o" points in the FGM, a simple linear interpolation is used between CGM points nearest the boundary FGM point rather than the "Lagrangian interpolation" used by Zhang et al. (1986). Second, no additional eddy diffusion is used in the region of the boundary at this stage of model development. This is a temporary modification so that any noise resulting from improper coding or inappropriate nesting criteria will be more apparent. Finally, the Newtonian damping scheme applied by Zhang et al. (1986) near the interface is not yet being employed for the same reason. We fully expect that the damping scheme and perhaps increased diffusion will be desirable in the final model to help reduce noise resulting from incompatibilities between the CGM and FGM solutions.

The model with nesting as described above is referred to as the horizontally and vertically nested model (HVN). Prior to completing a model version with the

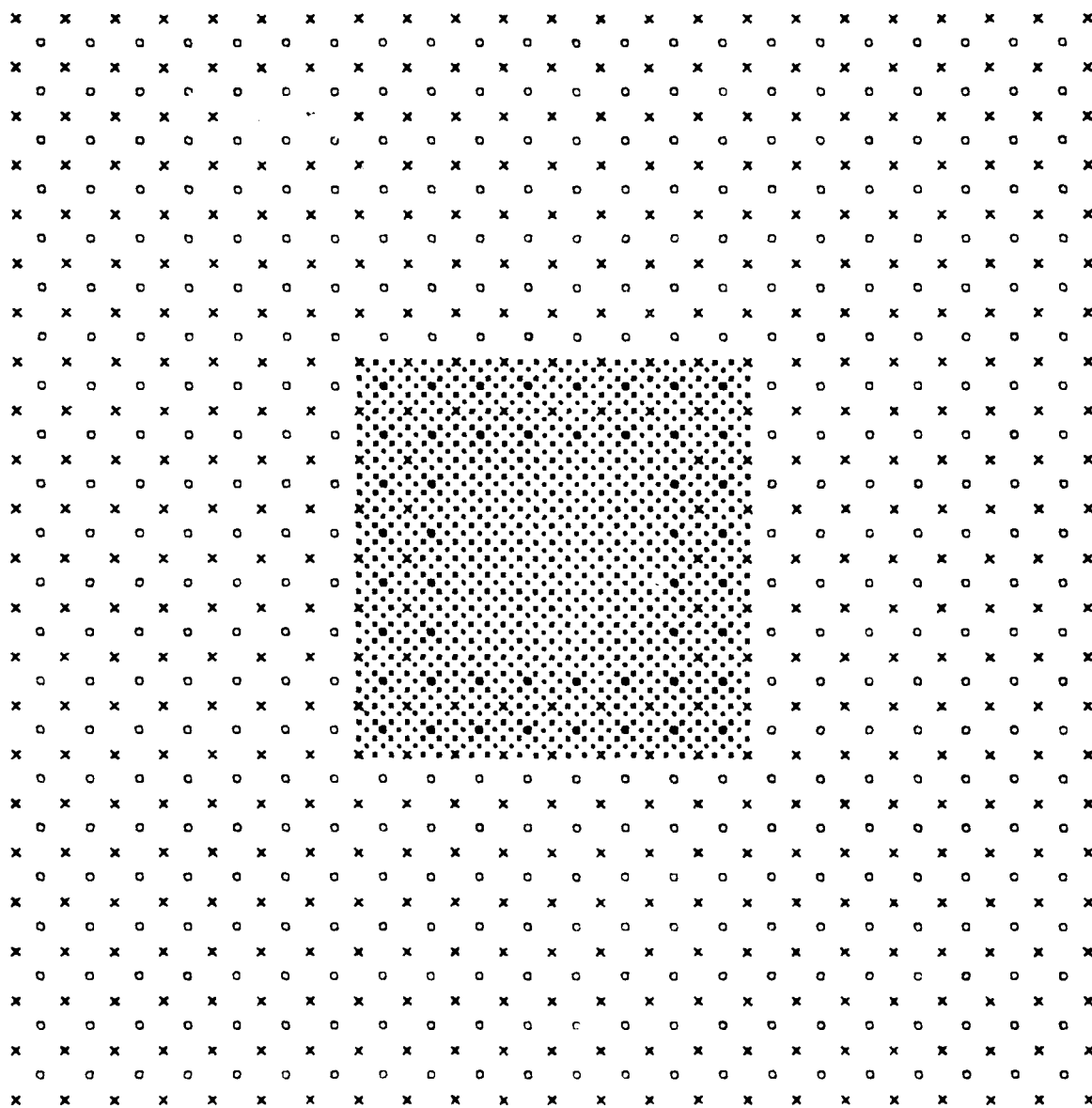


FIG. 2. Horizontal gridpoint structure for the nested model (HVN). Velocities are defined on "x" points and all other variables are defined on "o" points.

two-way interactive nesting of Zhang et al. (1986), a 20 km resolution model which employed only the vertical nesting was developed. This model, which had a domain size of 520 km x 520 km (for "o" points) is referred to as the vertical two-way interactive nesting model (VTWIN). Results of tests with both models will be presented in section 3.

It is possible to envision another degree of nesting beyond that in the HVN model which results in a considerable reduction of grid points, and hence a significant savings in computation time. Here, we retain the 20 km resolution FGM shown in Fig. 2 *only* for the two-layer model. The four-layer model uses a 60 km grid spacing over the entire CGM domain including the region "over" the FGM two-layer model. Philosophically, this structure represents a desire to achieve high resolution for boundary layer processes and acknowledges the much higher density of surface observations compared to upper air data. The vertical two-way interactive nesting is considerably more complicated for this configuration because it requires interpolation of coarse four-layer data to FGM points to serve as boundary values at the $\sigma_{k_{bm}}$ level and subsequent horizontal (as well as H -weighted vertical) averaging of two-layer variables to CGM points for feedback to the four-layer model. This nesting configuration results in an over-specification of the surface pressure variable, π , on the CGM points located coincident with FGM points. This over-specification, however, is no different from that which is present on CGM points in the interface region when the horizontal nesting procedure of Zhang et al. (1986) is used in a traditional nested model (or in HVN). Thus, it is hoped that with careful implementation the over-specification will be slight enough to allow successful integration. The nesting configuration described here, and referred to as horizontal and vertical nesting with no four-layer FGM (HVNNOFF), has not yet been tested. Its improvement in computation speed over the HVN model would be the result of a substantial decrease in gridpoints and also because CGM points (and hence the entire four-layer model) are only integrated once for every three time steps of the FGM points.

c. Other numerical details

Time integration for the model is performed using the leapfrog scheme with an Asselin filter. The time step for FGM points is 20 s and for CGM points is 60 s.

The flow relaxation condition of Davies (1976) is used on lateral boundaries following the work of Seitter (1987) who found that this condition was well-behaved, provided a simple means of allowing external information to be introduced into the model, and did not require the smoothing operator necessary in the Perkey and Kreitzberg (1976) sponge. The flow relaxation condition requires a 5 gridpoint wide region near the boundary for application, and solutions in this "relaxation region" should be considered modified. For the non-nested VTWIN model, this means that only the central 16×16 gridpoint mesh should be considered as having a true physical solution. For the HVN model, the relaxation region is contained in the CGM collar outside the CGM points providing boundary tendencies to the FGM. Therefore, the entire 24×24 FGM mesh can be viewed as a physical solution.

The last terms on the RHS of (2.2), (2.3) and (2.5) include a "friction" term, F , which, above the boundary layer, is given by horizontal eddy diffusion. This term is modeled by a simple Fickian diffusion, $K \nabla^2 \phi$, where K is a constant eddy viscosity and ϕ is the variable of interest (u , v , or T). In most simulations, we let $K = 2 \times 10^5 \text{ m}^2 \text{ s}^{-1}$ for the momentum components and $K = 0$ for temperature (see section 3 for a more complete discussion of the diffusion of temperature).

Several time-saving approximations are being introduced into the coding of the model. For example, energy conservation requires that the values of temperature used in the vertical advection term of the thermodynamic equation be found by taking the mean of the potential temperature (Anthes and Warner 1978). This requires the calculation of potential temperature at each mid-layer level, averaging these quantities to find an interface mean potential temperature, then using the Poisson equation to calculate the resulting interface temperature. Normally, this requires two calculations of quantities raised to non-integer power for each model layer, for each grid column, per time step. However, a small bias in the pressure level determination does not affect the potential temperature calculation substantially and that same bias is removed when conversion back to temperature occurs. Therefore, it is possible to calculate constant factors for each level at model initialization based on average surface pressure and use these factors in the average temperature calculation throughout the integration. This replaces the non-integer power calculation with one multiplication while producing no significant error.

The VAX VMS-Fortran compiler has a fairly effective optimization capability, and the model code is being written to take advantage of the optimizing routine as much as possible. This includes nesting DO-loops in a way that allows the machine-language code to employ auto-increment addressing and grouping variables to allow some precalculation at compilation time as well as register storage at execution time. The 32-bit word length of the VAX has shown up in noticable roundoff error in certain calculations. In several places in the model, special analytically equivalent forms of the equations have been used to minimize the impact of the roundoff error so that it cannot become a small but accumulating error in the model. One place where this showed up quite noticeably was in the application of the flow relaxation condition where even quiescent, horizontally homogeneous fields were being modified in the relaxation region unless the terms in the time-stepping equations were written to reduce their sensitivity to roundoff error.

3. Tests with the Model

a. Tests using VTWIN

Extensive tests were carried out with the non-nested model referred to as the VTWIN model. For all the tests described here, the model had no radiation or boundary layer parameterizations. The variable boundary layer height, σ_h , was set to a constant, normally halfway between the surface and $\sigma_{t_{bm}}$. Inspection of the equations given in section 2 reveals that the specification of σ_h as a constant reduces the two-layer model to a regular σ -coordinate model. The tests described here, therefore, were primarily designed to serve three purposes: 1) verify the basic coding of the model; 2) test the two-way vertical nesting scheme between the two-layer and four-layer models; 3) assess the impact of the coarse vertical resolution on the model's ability to simulate flow over complex terrain. Some additional tests, not described below in detail, were made with σ_h set so that one layer of the two-layer model was considerably thicker than the other. These simulations verified the consistency of the H -weighted vertical averages used to produce quantities required from the lowest layer of the four-layer model since changes in σ_h did not adversely affect the four-layer model solution.

After a series of geostrophic adjustment simulations with no terrain [similar to those of Seitter (1987)], a mountain ridge was added and tests were carried out on the model's ability to reproduce mountain lee-wave phenomena. The extremely coarse vertical resolution in the upper portion of the model was expected to severely limit its ability to reproduce mountain lee-waves. Interestingly, many features of lee waves were present in the simulations despite the inability of the model to properly resolve details of these features. Before summarizing the results of these tests, we will discuss a source of error in σ -coordinate models which does not appear to have an acceptable solution.

During the lee-wave testing, it became clear that extreme care must be exercised when applying an eddy diffusion to variables in a σ -coordinate model. Consider, for example, the eddy diffusion term applied to temperature. If this is handled as a simple Fickian diffusion in the form $K\nabla^2 T$, with the Laplacian evaluated on σ -surfaces, terrain features will induce an accumulating error which may eventually destroy the simulation through dynamical feedback. To see how this happens, imagine a σ -surface with a gridpoint directly above a peak. All surrounding gridpoints on the same model surface will be at a lower physical height because the σ -surface will deform with the terrain feature. Even if the temperature field is horizontally homogeneous (on constant height surfaces), a typical lapse rate with temperature decreasing with height will produce a somewhat higher value of T on the gridpoints surrounding the peak compared to that of the peak itself. Application of the Laplacian will produce a tendency in the thermodynamic equation which will raise the temperature on the point above the peak because the diffusion term will tend toward no gradients on sigma surfaces. This is, of course, an erroneous tendency which is an artifact of the simple treatment of the diffusion terms. If there is flow over the peak, which will tend to cool the air above the peak adiabatically, the error produced by the diffusion term will accumulate and prevent a steady state from being reached. This problem with the eddy diffusion terms will be most noticeable when trying to simulate nearly steady flow over complex terrain, so it surfaced early in test simulations of lee-wave phenomena.

The best way to reduce errors produced by the diffusion terms is not clear. One possibility would be to calculate diffusion on a constant pressure surface

through the gridpoint. This, however, requires an interpolation of the surrounding gridpoints' data from their σ -surface to the appropriate pressure surface and large truncation errors are likely to result -- especially if the model surfaces are not closely spaced in the vertical. Mellor and Blumberg (1985) suggest diffusion on σ surfaces, but only if K is a function of velocity so that K reduces to zero for zero velocity. This is the approach used in some other mesoscale models (e.g. Anthes and Warner 1978). It is easy to see that this does not eliminate the problem of error growth when the flow is nearly steady, unless the atmospheric lapse rate and the slope of a σ layer combine to yield a constant temperature on a σ -surface. The diffusion term could be reformulated in terms of potential temperature. This would reduce the problem in some types of flows but not for others, and would require a significant increase in computation for these terms. We anticipate that we will continue to apply a simple Fickian diffusion on σ -surfaces, but that we will set the diffusion coefficient, K , to be much smaller for all trace variables than the value used for momentum.

Unlike lee wave tests performed with other mesoscale models described in the literature (Anthes and Warner 1978; Nickerson et al. 1986), the tests described here were performed with the full three-dimensional model rather than a two-dimensional analog. A two-dimensional analog model requires a different gridpoint staggering since all points are in the plane. This means that the analog model is an inherently different model than the three-dimensional one. We feel it is better to test the full model directly. A mountain ridge was placed in the terrain field running north-south in the domain. The ridge height was reduced smoothly to zero in the vicinity of the north and south boundaries to reduce inconsistencies between the steady solution over the ridge and the boundary values which are held constant in the flow relaxation condition. This resulted in a ridge that was independent in the y -direction for the center 12 gridpoints in the domain. Solutions were displayed on an east west cross section through the center of the domain. The resulting flow should be similar to two-dimensional solutions in the literature (though not suffering from unrealistic two-dimensional constraints). These simulations provided a stringent test for the model.

Figure 3a shows the potential temperature field after 12 h of simulation for a 1 km Gaussian profile ridge. The u -component velocity field for this simulation is

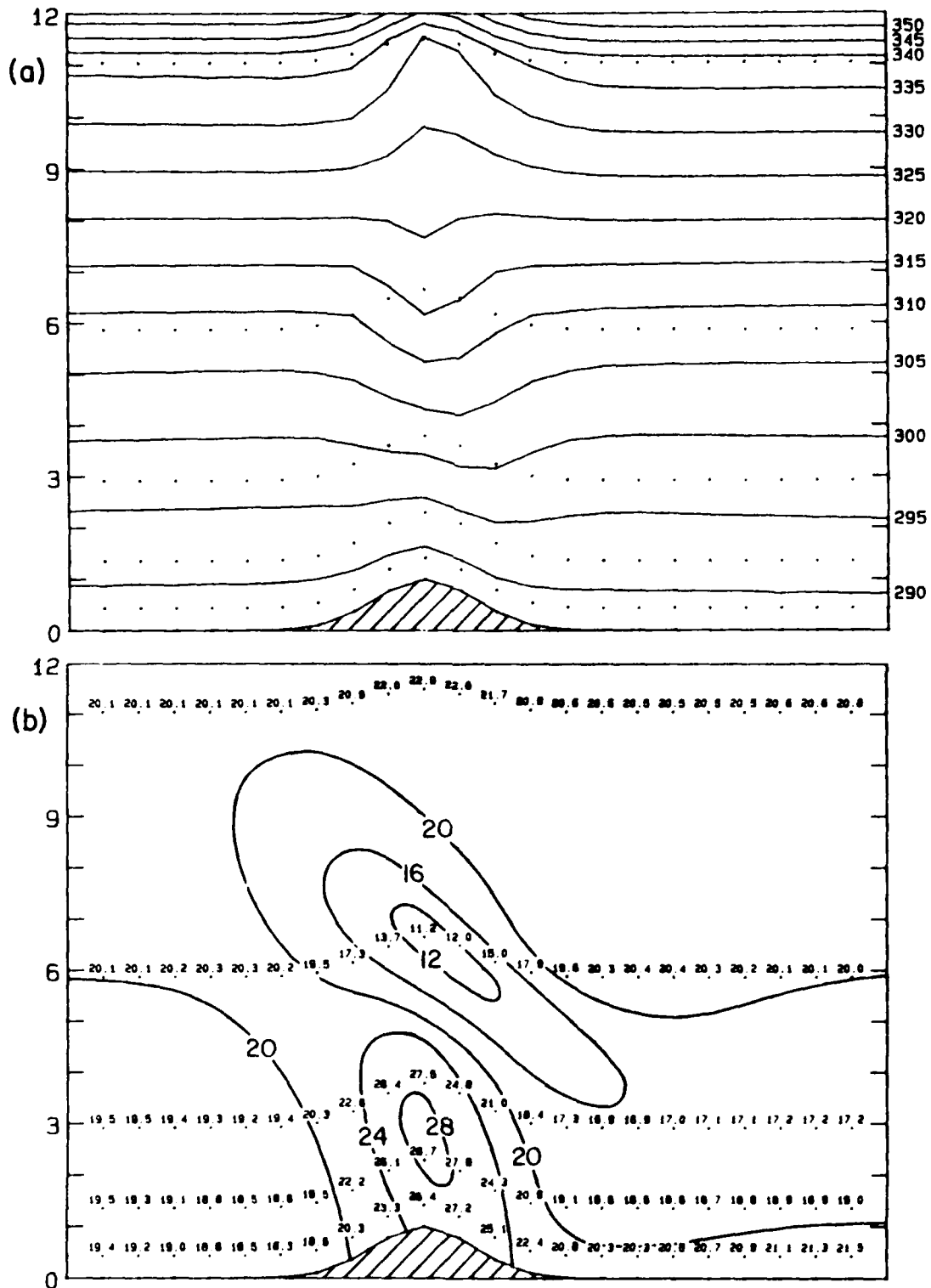


FIG. 3. East-west vertical cross-section through the center of the VTWIN model at 12 h simulated time showing (a) potential temperature and (b) u -component velocity. The scale along the left shows height in km, isentropes in panel (a) are labeled in K along the right boundary.

shown in Fig. 3b. The U.S. Standard Atmosphere temperature profile and 20 m s^{-1} u -velocity at all levels served as the initial conditions for these simulations and these values are held constant on all boundaries by the flow relaxation scheme. The Coriolis parameter was set to zero for these simulations in order to allow comparison between these tests and other published results. In Fig. 3a, the points show the positions of model gridpoints, with the plotted isentropes resulting from linear interpolation. In Fig. 3b, the velocity values are plotted at each gridpoint location and the contours have been subjectively analyzed. Clearly the coarse vertical resolution leads to a smoothing of the lee-wave structure, but comparison with a similar simulation by Nickerson et al. (1986, his Fig. 4a) shows that the major features are present - especially in the lower 6 km where the model resolution is better. A velocity maximum of over 30 m s^{-1} is located near the surface just downwind of the peak and a velocity minimum of less than 8 m s^{-1} is located at midlevels directly above the low level maximum. The velocity structure and potential temperature fields both show a distinct upwind tilt for the waves. There

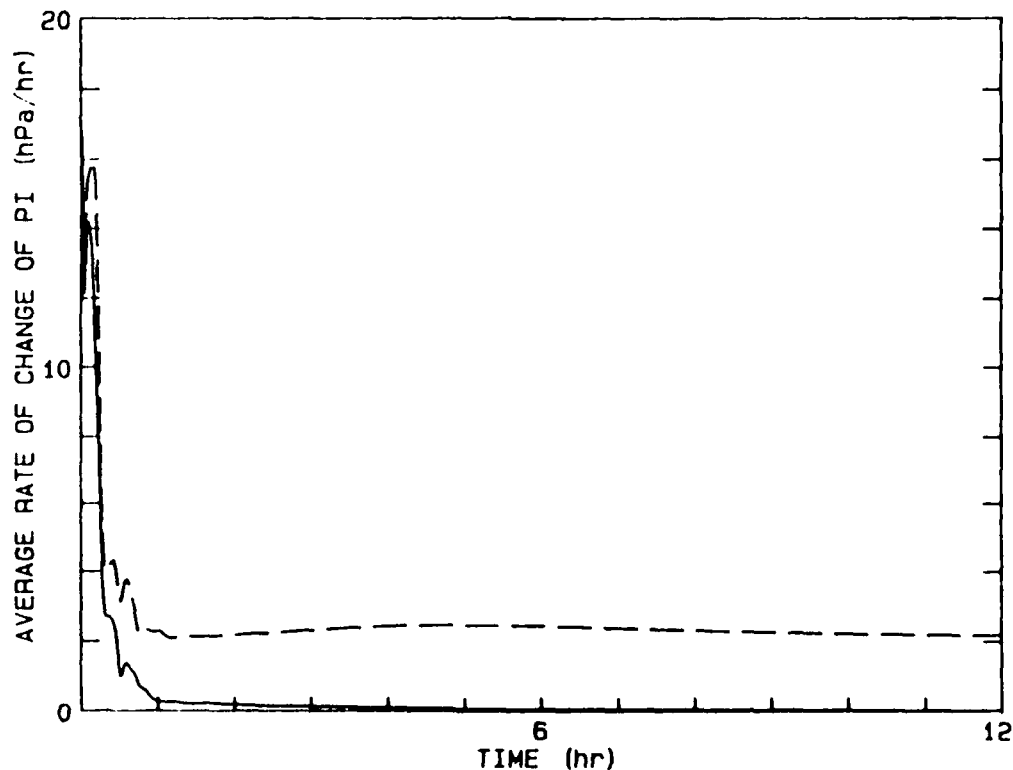


FIG. 4. Average rate of change of surface pressure for 12 h simulation shown in Fig. 3.

is no damping layer in the upper portion of the model, so the amplitude of the wave is larger there than it should be. Unlike the Nickerson et al. (1986) solution, the model has no frictional boundary layer for these tests, so the velocities are carried down to the surface.

Figure 4 shows a plot of the average rate of change of the surface pressure for the 12 h of the simulation shown in Fig. 3. The dashed curve is the average of $d\pi/dt$ over the domain before the application of the flow relaxation condition. A zero value for this quantity indicates perfect dynamic balance within the model domain. It does not reach perfect balance because the boundary values are not exactly consistent with the lee-wave solution. The solid curve represents the average over the domain of $d\pi/dt$ after the application of the boundary condition [see Seitter (1987) for a more complete discussion of the difference between these two quantities]. A value of zero for this quantity indicates a perfectly steady solution. This figure indicates a period of adjustment within the model for the first hour during which the flow becomes nearly balanced (except for the gridpoints in the flow relaxation region near the boundaries). After the first hour the model solution is very steady.

Other test simulations with lee-wave phenomena included varying the width and sharpness of the mountain ridge, varying the stability, and varying the eddy coefficient. The solution changed in only minor ways with changes in the mountain shape or atmospheric stability and always in ways consistent with lee-wave theory. Reduction of the eddy diffusion coefficient for momentum by a factor of 10 or more resulted in short wavelength noise being generated, especially upwind of the mountain. This is thought to be primarily an artifact of the closeness of the upwind boundary and interactions between the boundary condition and the flow. However, Anthes and Warner (1978) indicate that low resolution in the vertical requires a nondimensional eddy coefficient of about 0.01 in order for a reasonable solution to be produced when no upper damping layer is present in the model. The solution shown in Fig. 3 was produced with a nondimensional eddy coefficient of 0.005.

The solutions from these tests are quite good in the lower troposphere where the emphasis of the model is being placed. Clearly, the model is incapable of being used to investigate the details of lee-wave phenomena, but we are very encouraged

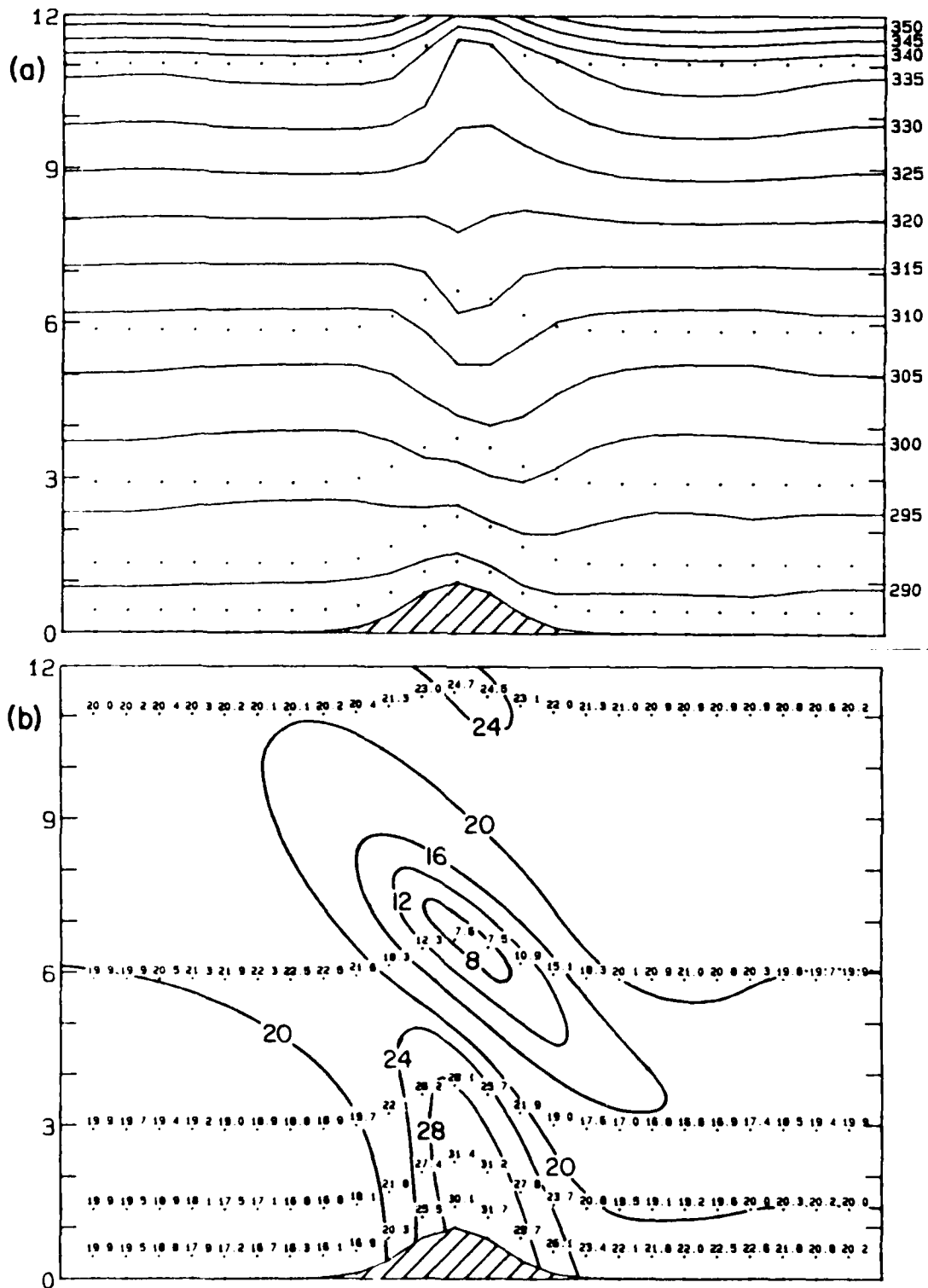


FIG. 5. Fast-west vertical cross-section through the center of the HVN model fine grid mesh at 12 h simulated time showing (a) potential temperature and (b) u -component velocity.

by its ability to capture those features which will impact the forecast at lower levels during these events.

b. Tests with the HVN model

Mountain lee-wave simulations similar to the ones described above (as well as geostrophic adjustment and other tests) have also been performed with the horizontally nested HVN model. As in the non-nested simulations, a north-south mountain ridge of 1 km height was placed in the domain. The northern and southern ends of the ridge sloped smoothly to zero height and the ridge was designed to fit in only the FGM domain (though its northern and southern ends extended somewhat into the overlapping feedback region of the CGM). The resulting ridge had a constant height over 10 gridpoints in the y -direction. Simulations out to 12 h were carried out for several ridge profiles.

Figure 5a shows an east-west cross-section of potential temperature at 12 h in the FGM domain for the same Gaussian profile ridge as shown in Fig. 3a. These results appear very similar to those of the non-nested model. Despite the lack of diffusion on temperature and no Newtonian damping term near the boundary, the solution is quite well-behaved. The cross-section of u -velocity for this simulation, shown in Fig. 5b, shows that the lee-wave has a smaller amplitude than that of the non-nested simulation. This appears to be related to the close lateral boundaries in the non-nested model which held the velocity fixed at 20 m s^{-1} . The nested model allows the velocity to adjust at the FGM boundary and it appears that the wave took on a broader structure of lower amplitude when not constrained by the flow relaxation condition on FGM boundaries.

To show the smoothness of the solution at the interface between the CGM and FGM, Fig. 6 shows a vertical cross-section of potential temperature through the CGM domain. The extent of the FGM domain is shown by the vertical dashed lines, and the values plotted within this region were obtained by applying the same 9-point operator that is used to provide feedback from the FGM to the CGM in the two-way interactive nested procedure (Zhang et al. 1986). Comparison of Figs. 5a and 6 show that the lee-wave structure would not be resolved very well by a 60 km resolution model. This did not, however, lead to an incompatibility between the FGM and CGM solutions at the interface, so no discontinuities are apparent.

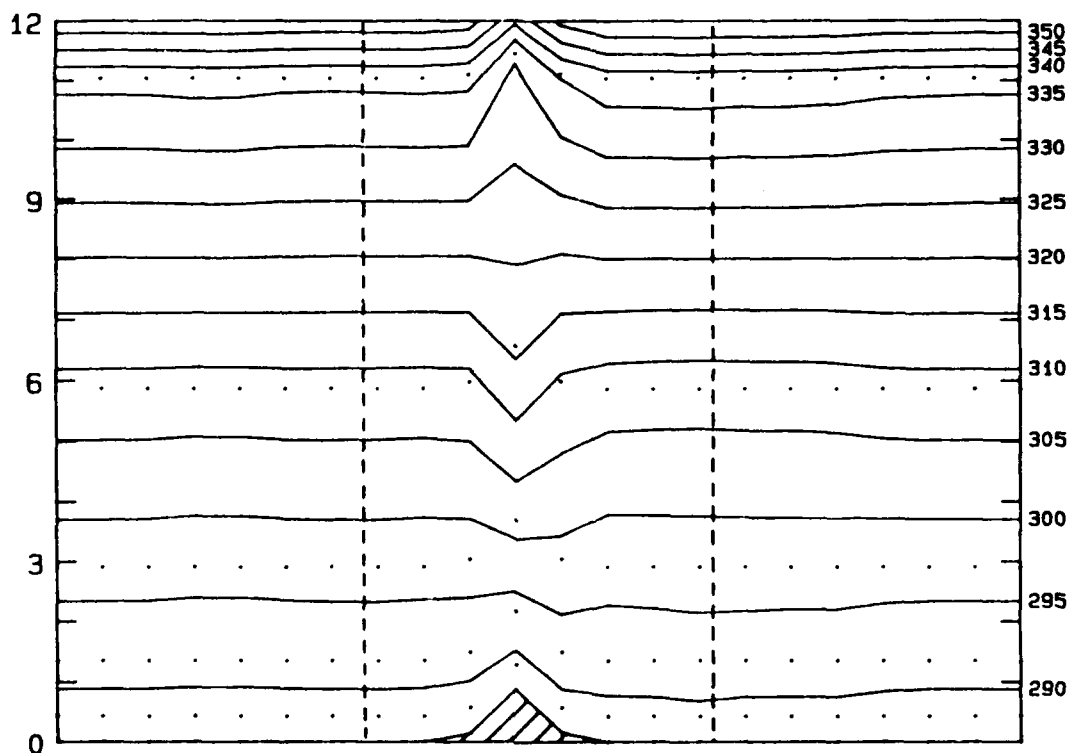


FIG. 6. East-west vertical cross-section through the center of the HVN model coarse grid mesh at 12 h simulated time showing potential temperature.

Figure 7 shows the variation with time of the FGM domain average rate of change of surface pressure, $|\frac{d\pi}{dt}|$, for the 12 h simulation shown in Fig. 5. Comparison with Fig. 4 shows that the nested model requires a somewhat longer time to reach a nearly steady state (about 2 h) and undergoes larger oscillations while adjusting. This is clearly related to the lack of damping in the FGM of the nested simulation compared to that provided by the flow relaxation condition in the non-nested model. It would also appear that Lamb waves produced during the adjustment period suffer partial reflection at the FGM-CGM interface due either to aliasing of the waves or as a result of the over-specification of the pressure in the FGM-CGM overlap region. Still, the model appears quite stable — even this version which has little means of removing noise in the FGM. This is very encouraging and suggests that even though the coarse vertical resolution of the model fails to adequately resolve the details of the lee-wave phenomena, there is no reason to fear that topographically induced waves will lead to disturbances which will destroy other aspects of the simulation.

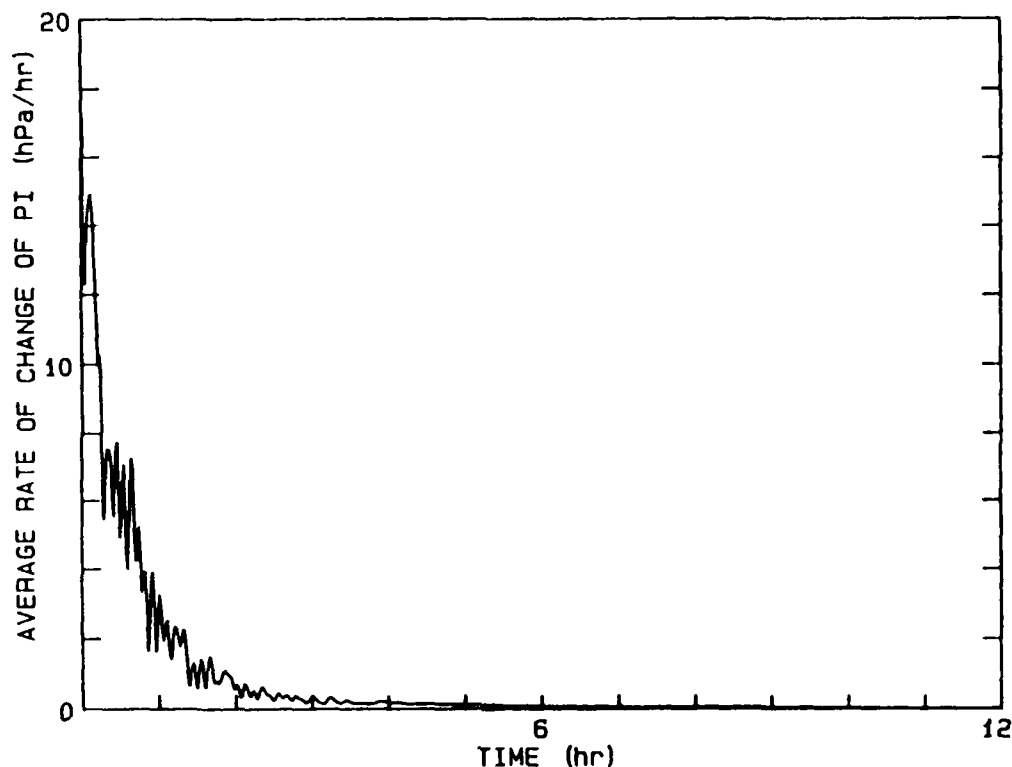


FIG. 7. Average rate of change of surface pressure in FGM for 12 h simulation shown in Fig. 5.

Despite the considerable increase in the size of the physical domain for the nested model and the added complexity of the horizontal nesting procedure, the HVN model runs in nearly the same amount of time as the non-nested VTWIN model (just under 1 h CPU time for a 12 h simulation on a MicroVAX 3). This is partly a result of coding improvements made to the HVN model which were not utilized in VTWIN. Mostly, however, the comparable speed is a result of two aspects of the nesting itself. First, the FGM of the HVN has only a 24×24 gridpoint domain (for "o" points) compared to the 26×26 domain of the VTWIN model, so HVN has about 15% fewer gridpoints at 20 km resolution. Second, the 60 km resolution CGM points surrounding the FGM in HVN are only integrated once for every 3 timesteps of the FGM (and the CGM collar only requires integration on about 2/3 as many points as the FGM). It seems clear that the nested HVN model is preferable to the non-nested VTWIN, and does not increase computation time enough to threaten the operational goal of this project.

4. Boundary layer parameterization

All of the test simulations described in the previous section were carried out in versions of the model which had a constant boundary layer height, σ_h . As stated in section 2, however, a major component of this work is the development of a model with variable-height boundary layer. The formulation of the boundary layer parameterizations which will be incorporated into the model described above is presented in this section. The boundary layer parameterization is composed of several parts: radiation; surface energy and moisture balance; boundary layer height; and boundary layer air temperature and specific humidity. Each of the formulations, described in the following subsections, is designed to balance computational speed with physical accuracy. In most cases, the physical accuracy is restricted by the limited vertical resolution of the model rather than by the mathematical formulation.

a. radiation

The radiation parameterization is taken from Katayama (1972) and is a routine originally designed for use in the UCLA GCM. The incident radiation and infra-red (IR) emission are calculated separately. The model incorporates an exponential fit to the data for specific humidity to allow simple integration of water content. CO_2 is included in a fixed form based on experimental data, and its contribution is then a constant.

The influx of radiation is computed by starting with the solar constant and modifying it for albedo at the top of the atmosphere. Scattered and absorbable radiation are computed separately, the fraction being assumed constant (35% available for absorption, 65% scattered to the ground). The scattered part of the incident radiation is corrected for multiple reflection between the atmosphere and the ground and given by

$$GLW_s = (.651)S_0 \cos ZT \left\{ \frac{1 - \alpha_s}{1 - \alpha_s \alpha_g} \right\} \quad (4.1)$$

where

S_0 = solar constant as a function of day of year

ZT = zenith angle for time of day and location

α_s = scattering albedo for the atmosphere (if clouds are present they determine the scattering albedo)

α_g = albedo of ground surface as a function of hour angle and surface characteristics (Wetzel 1978)

If a cloud layer is present, its presence is felt by both scattered and absorbable components. If the cloud is thick enough, and covers enough sky, incident radiation can be shut off. The model allows for variable amounts of cloud in each atmospheric layer expressed as a percentage. Only one layer of cloud is allowed, but it may be composed of one or several atmospheric layers of various percentage coverage.

Fractional absorption by water vapor is calculated by

$$ABS(i) = (0.271) \left[\frac{E_{H_2O}(i)}{\cos(ZT)} \right]^{0.303} \quad (4.2)$$

where E_{H_2O} is the effective amount of water vapor in layer i . The radiation which finally is absorbed in the soil becomes one component of the surface energy balance. The absorbed part of the incident radiation at the ground is

$$GLW_s = (0.349 S_0 \cos ZT) - \sum_i ABS(i) \quad (4.3)$$

where the sum is taken over all layers. The total absorption at the ground is then

$$GAB = (1 - \alpha_g)(GLW_s + GLW_a) \quad (4.4)$$

To find the IR flux, the equation of radiative transfer is solved subject to the boundary conditions that downward IR flux at the top of the atmosphere is zero, and the upward IR flux at the earth's surface is the black-body radiation at the surface temperature. Weighted transmission functions are used, corrected for the pressure dependence of absorption by defining an effective amount of an absorber. The total transmission function is assumed to be the product of the individual ones for CO_2 and H_2O . Downward flux is

$$IR_d = \tau B_z + \tau B \cdot \bar{\tau}(u_\infty^* - u_z^*, T_z) - (\tau B_\infty - \tau B_z) \tau(u_\infty^* - u_z^*, \bar{T}) \\ + \int_{\tau B_z}^{\tau B_\infty} \tau(u^* - u_z^*, \bar{T}) d(\tau B) \quad (4.5)$$

where

$$\tau B_i = \sigma T_i^4$$

σ = Stephan-Boltzmann constant

$\bar{\tau}, \tau$ = mean total transmission functions for effective absorber u^* at temperature T

T_c = critical temperature which divides the region of weak temperature dependence of τ to that of strong dependence of τ .

The weak region is 210-320 K for water vapor, so letting $T_c = 220$ K, the weak dependence region need only have a mean temperature specified (\bar{T}). Similarly, the upward flux is

$$IR_u = \tau B_z + \int_{\tau B_z}^{\tau B_g} \tau(u^* - u_z^*, \bar{T}) d(\tau B) \quad (4.6)$$

and the net upward flux is

$$IR_z = IR_u - IR_d \quad (4.7)$$

The only difficulty is determining the proper transmission function near the particular level where τ varies exponentially. The model uses an interpolation factor which is an empirical function of pressure, mixing ratio and layer thickness. This allows proper calculation of τ without a fine vertical mesh. The mean transmission functions are defined by empirical formulae at $T_c = 220$ K and $\bar{T} = 260$ K. Temperature dependence of τ for CO_2 is neglected, so a mean τ for CO_2 is used based on pressure and amount of CO_2 . The distribution of CO_2 at each level is a constant.

The IR flux is computed only for the surface, since the IR cooling rates in the free atmosphere are insignificant on diurnal time scales. This saves

considerable computation time. The net radiation is then

$$NR = GAB - IR_s \quad (4.8)$$

Radiation calculations were made with the above scheme for a varying number of atmospheric layers. These calculations showed that when layers were thicker than 100 mb, errors occurred in the net radiation values. Comparisons were made, for example, using a sounding that originally had 19 unevenly spaced levels. Reducing this to only 7 levels produced NR values in error by nearly 15%. If, however, the routine started with the same 7 levels but was allowed to linearly interpolate a new level in the middle of any layer thicker than 100 mb, the error in NR was reduced to less than 10% — despite the fact that no additional vertical resolution in temperature was available.

b. surface energy balance

The surface energy balance has the form

$$NR = SH + LH + GS \quad (4.9)$$

where NR is the net radiation incident on the surface (as defined in the previous subsection), SH is the sensible heat flux upward from the surface, LH is the latent heat flux upward from the surface, and GS is the soil heat flux downward into the ground (heating the soil). The NR value is determined from the radiation parameterization [see eq. (4.8)]. The other terms are parameterized as follows.

The sensible heat flux and latent heat flux (SH , LH) are parameterized using Monin-Obukhov similarity theory for the planetary boundary layer (PBL). The fluxes depend on the vertical gradients of temperature and specific humidity in the surface layer, the surface geostrophic wind, and the stability of the boundary layer. The theory assumes that the structure of temperature and moisture in the PBL have forms which can be described by universal structure functions when scaled equations are used. There are actually two structures involved, since the PBL contains at least two distinct layers — the surface layer and the boundary layer. Although the two-layer model structure does not include an explicit surface

layer, one is assumed to be present by the parameterization. This "surface layer" is assumed to be a constant 5 mb thick. If the functions are required to be matched at their common boundary, the following results are obtained

$$\frac{u_{g0}}{u_*} = \frac{1}{k} \left[\ln \left| \frac{u_*}{f z_0} \right| - A(\mu) \right] \quad (4.10)$$

$$\frac{v_{g0}}{u_*} = - \frac{B(\mu)}{k} \text{Sign} f \quad (4.11)$$

$$\frac{\theta_\infty - \theta_0}{\theta_*} = \frac{1}{k} C \left[\ln \left| \frac{u_*}{f z_0} \right| - C_1(\mu) \right] \quad (4.12)$$

$$\frac{u_{g0}}{u_*} = \frac{1}{k} \left[\ln \frac{h}{z_0} - A_1(\mu) \right] \quad (4.13)$$

$$\frac{v_{g0}}{u_*} = - \frac{B_1(\mu)}{k} \text{Sign} f \quad (4.14)$$

$$\frac{\theta_\infty - \theta_0}{\theta_*} = \frac{1}{k} C \left[\ln \frac{h}{z_0} - C_1(\mu) \right] \quad (4.15)$$

where

u_{g0}, v_{g0} = components of the surface geostrophic wind

θ_∞ = potential temperature at the top of the PBL

θ = potential temperature at the ground

$\theta_* = -SH/u_*$

u_* = friction velocity

k = von Kármán's constant

C = dimensionless constant

$\mu = ku_*/fL$

$\mu_1 = h/L$

f = Coriolis parameter

L = Obukhov's length

z_0 = roughness length (function of location)

h = height of the boundary layer

and

$A(\mu), B(\mu), C(\mu)$ = universal functions for a stable boundary layer

$A_u(\mu), B_u(\mu), C_u(\mu)$ = universal functions for an unstable boundary layer

where the universal functions are those given by Arya (1975).

To determine the fluxes, we use inverted forms of these equations which are based on two parameters:

$$\text{stable case} \quad S = \frac{g(\theta_\infty - \theta_0)}{\theta |f| G_c} \quad (4.15)$$

$$\text{unstable case} \quad S_i = \frac{g(\theta_\infty - \theta_0)h}{G_c^2} \quad (4.16)$$

and

$$\text{stable and unstable} \quad R_c = \frac{G}{|f| z} \quad (4.17)$$

where

G_c = surface geostrophic windspeed

g = acceleration of gravity

θ = mean potential temperature.

The inverted equations have the form

$$\frac{T_{01}}{\rho G_c^2} = C_f(R_c, S) \quad (4.18)$$

$$\tan^{-1} \left(\frac{v_{y0}}{u_{y0}} \right) = \alpha_0(R_c, S) \quad (4.19)$$

$$\frac{SH}{G_c(\theta_\infty - \theta_0)} = C_h(R, S) \quad (4.20)$$

where τ_0 is the surface stress and ρ is the density of air. The latent heat flux (LH) is computed by assuming that it obeys the universal function for SH, that is,

$$\frac{q_{\infty} - q_0}{q_*} = \frac{\theta_{\infty} - \theta_0}{\theta_*} \quad (4.21)$$

where q is the specific humidity and

$$q_* = \frac{LH}{u_*} \quad (4.22)$$

c. ground variables

Ground temperature (TG) and ground wetness (GW) are parameterized by "force restore" methods from Bhumralker (1975) and Deardorff (1977). Following Bhumralker (1975), heat conduction in the soil is described by

$$\frac{\partial T_g(z,t)}{\partial t} = \frac{\kappa}{c} \frac{\partial^2 T_g(z,t)}{\partial z^2} \quad (4.23)$$

where

$T_g(z,t)$ = soil temperature at depth z , time t

κ = thermal conductivity of soil

c = volumetric heat capacity.

We assume that TG is described by

$$TG = \bar{T} + \Delta T_g \sin(\omega t) \quad (4.24)$$

where

\bar{T} = average temperature of the soil, assumed to be invariant with depth (in practice, the 50 cm soil temperature is used)

ΔT_g = amplitude of the variance

ω = frequency of the variance.

Then the solution of (4.23) is

$$T_g(z,t) = \bar{T} + \Delta T_0 \exp(-z/d) \sin(\omega t - z/d) \quad (4.25)$$

where $d = (\kappa/c\omega)^{1/2}$ is the depth at which the amplitude of ΔT_g is negligible. For an infinitely thin soil layer, the heat flux into the soil at depth z is

$$G(z,t) = -\kappa \frac{\partial T_g(z,t)}{\partial z} \quad (4.26)$$

Combining (4.25) and (4.26) gives

$$G(z,t) = \left(\frac{\omega c \kappa}{2}\right)^{1/2} \Delta T_0 e^{-z/d} [\sin(\omega t - z/d) + \cos(\omega t - z/d)] \quad (4.27)$$

Eliminating ΔT_0 , one obtains

$$G(z,t) = \left(\frac{\omega c \kappa}{2}\right)^{1/2} \left[\frac{1}{\omega} \frac{\partial T_g(z,t)}{\partial t} + T_g(z,t) - \bar{T} \right] \quad (4.28)$$

Consider a layer of soil from the surface ($z = 0$) to some depth z . The time rate of temperature change for this layer is given by

$$c \frac{\partial T_g(z,t)}{\partial t} = - \left[\frac{G(z,t) - GS}{z} \right] \quad (4.29)$$

If the approximation is made that

$$T_g(z=1 \text{ cm}, t) \approx TG \quad (4.30)$$

then (4.29) becomes (with the use of (4.9)),

$$\left[c + \left(\frac{c\kappa}{2\omega}\right)^{1/2} \right] \frac{\partial TG}{\partial t} = GS - \left(\frac{\omega c \kappa}{2}\right)^{1/2} (TG - \bar{T}) \quad (4.31)$$

or

$$\frac{\partial TG}{\partial t} = \left[GS - \left(\frac{\omega c \kappa}{2}\right)^{1/2} (TG - \bar{T}) \right] \left[c + \left(\frac{c\kappa}{2\omega}\right)^{1/2} \right]^{-1} \quad (4.32)$$

The surface soil moisture (GW) is found by assuming that it changes due to three main processes -- precipitation, evaporation, and flux from below. The bulk soil moisture (GW_B) is assumed to be constant over the period. According to Deardorff (1977) the bulk soil moisture changes over a time scale of a few weeks, so GW_B can certainly be assumed constant for a 24 h period with little loss of accuracy. The surface soil moisture is changed according to

$$\frac{\partial GW}{\partial t} = \frac{c_1(LH/\lambda - P_r)}{\rho_w d_1 W_{max}} - \frac{c_2(GW - GW_B)}{\tau} \quad (4.33)$$

where

GW_B = percent bulk soil saturation (top 50 cm)

GW = percent surface soil saturation

d_1 = depth of diurnal cycle (= 10 cm)

λ = latent heat of evaporation

ρ_w = density of water (1 gm cm⁻³)

W_{max} = field capacity soil moisture

τ = period of cycle

c_1, c_2 = nondimensional constants

P_r = precipitation rate.

Deardorff's values for c_1 and c_2 were computed from data of Jackson (1973), measurements taken over bare soil near Phoenix, Arizona in March. This gives

$$c_1 = \begin{cases} 0.5 & GW > 75\% \\ 14 - 22.5(GW - 0.15) & 15\% < GW < 75\% \\ 14 & GW \leq 15\% \end{cases} \quad (4.34)$$

$$c_2 = 0.9$$

Notice that the middle value of c is a linear interpolation between the two extremes.

d. boundary layer height

1) unstable boundary layer

The unstable PBL is assumed to be well mixed below an inversion characterized by a jump discontinuity in potential temperature ($\Delta\theta$). The depth of the unstable boundary layer, h , and the strength of the inversion, $\Delta\theta$, are predicted according to Zeman and Tennekes (1977). Their method assumes that the PBL depth changes due to turbulent entrainment of air above the inversion into the PBL. The energy comes from the virtual SH flux at the surface, and the change of depth with time depends on the strength of the inversion. They use the turbulent kinetic energy (TKE) budget to develop a simple set of equations to describe this process.

The sensible heat flux at the inversion is equal to the temperature jump, $\Delta\theta$, times the rate of rise of the inversion

$$VSH_i = \Delta\theta \frac{\partial h}{\partial t} \quad (4.35)$$

where VSH_i is the virtual sensible heat flux at the inversion. The inversion strength changes as a function of entrainment of stable air from above, and net sensible heat transfer inside the boundary layer. It is given by

$$\frac{\partial \Delta\theta}{\partial t} = \gamma \frac{\partial h}{\partial t} - VSH + VSH_i / h \quad (4.36)$$

where VSH is the virtual sensible heat flux at the surface and γ is the potential temperature lapse rate above the PBL. The TKE budget can be written as

$$\frac{\partial TKE}{\partial t} = \text{production} + \text{transfer} - \text{dissipation} \quad (4.37)$$

which can be expanded into

$$C_z \frac{w_*^2}{h} \frac{\partial h}{\partial t} = \frac{g}{T_S} VSH + C_f \frac{w_*^2}{h} - C_d w_*^2 \omega_{bv} \quad (4.38)$$

where

$$w_* = \text{convective velocity scale} = \left[\frac{g}{TS} VSH h \right]^{\frac{1}{2}}$$

$$\omega_{bv} = \text{Brunt-Vaisala frequency} = \left(\frac{g\gamma}{TS} \right)^{\frac{1}{2}}$$

TS = temperature at the top of the surface layer

and C_r , C_f , and C_t are dimensionless constants. Substituting for $\partial h / \partial t$ from (4.35) yields

$$- \frac{g}{TS} VSH h = \frac{w_*^3}{h} \left[C_f - C_d \omega_{bv} \left(\frac{h}{w_*} \right) \right] \left[1 + \frac{C_t w_*^2 TS}{g \Delta \theta h} \right]^{-1} \quad (4.39)$$

Substituting for w_* gives

$$- \frac{VSH h}{VSH} = \left[C_f - C_d \omega_{bv} \left(\frac{h}{w_*} \right) \right] \left[1 + \frac{C_t w_*^2 TS}{g \Delta \theta h} \right]^{-1} \quad (4.40)$$

The values of the dimensionless coefficients C_d , C_f , and C_t are taken to be (Zeman 1975)

$$\begin{aligned} C_d &= 0.024 \\ C_f &= 0.50 \\ C_t &= 3.55 \end{aligned} \quad (4.41)$$

We can write the rate of change of boundary layer height as

$$\frac{\partial h}{\partial t} = - \frac{VSH h}{\Delta \theta} \quad (4.42)$$

In the case where $\Delta \theta = 0$, no inversion exists and the atmosphere presents no barrier to inversion rise. In this case, the model assumes a very small value for $\Delta \theta$, since the inversion must rise at a rapid but finite rate due to turbulent entrainment.

2) stable boundary layer

The depth of the stable boundary layer is calculated using a parameterization from Yamada (1979) that starts with the thermal energy equation

for flat terrain,

$$\frac{\partial \theta}{\partial t} = \frac{\partial}{\partial z}(-SH_z) + \left(\frac{\partial \theta}{\partial t}\right)_r \quad (4.43)$$

where SH_z is the sensible heat flux at level z and $(\partial \theta / \partial t)_r$ is the rate of change of temperature due to longwave radiation. Integrating this between the surface and the top of the boundary layer, h , yields

$$\int_0^h \frac{\partial \theta}{\partial t} dz = SH_s - SH_h + \int_0^h \left(\frac{\partial \theta}{\partial t}\right)_r dz \quad (4.44)$$

where the subscript s refers to the surface (actually, the top of the surface layer) and subscript h refers to the top of the boundary layer. If we assume that the vertical profile of potential temperature has a simple cubic form, increasing upwards (supported by observations), the equation can be integrated to yield

$$\int_0^h \frac{\partial \theta}{\partial t} dz = \frac{1}{4}(\theta_s - \theta_h) \frac{dh}{dt} + \frac{h}{4} \left(3 \frac{\partial \theta_s}{\partial t} + \frac{\partial \theta_h}{\partial t} \right) \quad (4.45)$$

Since turbulence in a stable PBL decreases rapidly with height, at the top of the PBL $SH=0$, so (4.43) becomes

$$\left(\frac{\partial \theta}{\partial t}\right)_r = \frac{\partial \theta_h}{\partial t} \quad (4.46)$$

At the surface, the cooling of the air is taking place primarily by radiation, so (4.43) becomes

$$\left(\frac{\partial \theta}{\partial t}\right)_r = \frac{\partial \theta_s}{\partial t} \quad (4.47)$$

Linearly interpolating between these two expressions gives

$$\left(\frac{\partial \theta}{\partial t}\right)_r = \frac{\partial \theta_s}{\partial t} \left(1 - \frac{z}{h}\right) + \frac{\partial \theta_h}{\partial t} \frac{z}{h} \quad (4.48)$$

Equation (4.44) then becomes

$$\int_0^h \frac{\partial \theta}{\partial t} dz = SH_s - SH_h + \frac{h}{2} \frac{\partial \theta_s}{\partial t} + \frac{h}{2} \frac{\partial \theta_h}{\partial t} \quad (4.49)$$

The change of potential temperature above the PBL is much smaller than the change at the surface, so $(\partial \theta_h / \partial t) \approx 0$. Further, SH_h is typically much smaller than SH_s , it, too, can be set to zero as a good approximation. Equating (4.45) and (4.49), we obtain the rate equation for the stable PBL depth

$$\frac{dh}{dt} = \frac{-1}{\theta_h - \theta_s} \left[h \frac{\partial \theta_s}{\partial t} + 4(SH_s) \right] \quad (4.50)$$

e. boundary layer variables

The surface temperature is found as a by-product of the PBL depth calculations. For the unstable PBL, we proceed as follows:

$$\Delta \theta_p = \theta_i + \frac{z_t - \Delta h}{z_t} (\theta_p - \theta_i) - \theta_r \quad (4.51)$$

where

θ_p = potential temperature above jump discontinuity

θ_i = potential temperature of the free atmosphere above the PBL

z_t = thickness of the next model layer above the PBL

Δh = change in PBL depth over one time step.

The potential temperature at the top of the 5 mb surface layer is given by

$$\theta_s = \theta_L - \Delta \theta \quad (4.52)$$

which allows the surface temperature to be found by Poisson's equation as

$$TS = \theta_s \left[\frac{p_{sfc} - 5}{1000} \right]^{0.286} \quad (4.53)$$

For the stable PBL, we start in a similar manner, except that there is no inversion jump discontinuity. We simply interpolate in potential temperature between the PBL top and the ground to find θ , then compute TS with (4.53).

For humidity, a moisture budget is used for both stable and unstable PBLs. This budget can be written

$$\frac{\partial q}{\partial t} = \left[\begin{array}{c} \text{flux of moisture} \\ \text{into PBL} \end{array} \right] + \left[\begin{array}{c} \text{entrainment of moisture} \\ \text{from above PBL} \end{array} \right] . \quad (4.54)$$

The flux of moisture is given by LH , and the entrainment of moisture is a result of the growth of the PBL and thus a function of Δh . The rate of change of specific humidity given by (4.54) is then used in the model equation governing the change of specific humidity.

5. Conclusions and Future Work

The problem of developing a meso- β numerical model capable of providing operational forecast guidance while running on a super-micro class computer is not an easy one. The model described in this report appears to be one possible solution for this problem. While much simpler than most mesoscale models, it still attempts to treat important physical processes in a realistic way — though much differently from other mesoscale models. The coarse vertical resolution is clearly a sacrifice, but tests indicate that the model is stable and well-behaved even while simulating flow over complex terrain. It is noteworthy, in regard to this point, that early versions of the PSU/NCAR mesoscale model had nearly the same vertical resolution as the model developed here.

A major aspect of the model development, the variable depth boundary layer formulation of the two-layer model, has not been tested within the three-dimensional model. One-dimensional testing of the boundary layer parameterizations has produced realistic results, but examination of the usefulness of the η -coordinate as a means of representing a variable-depth model layer within a three-dimensional model awaits the completion of the integration of the parameterization into the complete model. This is being worked on at the writing of this report, and represents the first stage of future work on the model.

Other future work includes the addition of moisture to the model. The equations for humidity are being added at the same time as the boundary layer and radiation parameterizations so that the humidity variables required for these packages are present. Prognostic equations for clouds and precipitation will not be included until extensive testing for clear-sky conditions has been completed. These tests will include such phenomena as the development of the sea-breeze, diurnal variation of the boundary layer, and diurnal mountain-valley circulations.

References

- Anthes, R.A., and T.T. Warner, 1978: Development of hydrodynamic models suitable for air pollution and other mesometeorological studies. *Mon. Wea. Rev.*, **106**, 1045-1078.
- Arya, S.P.S., 1975: Geostrophic drag and heat transfer relations for the atmospheric boundary layer. *Quart. J. Roy. Meteor. Soc.*, **101**, 147-161.
- Bhumralker, C.M., 1975: Numerical experiments on the computation of ground surface temperature in an atmospheric general circulation model. *J. Appl. Meteor.*, **14**, 1246-1258.
- Davies, H.C., 1976: A lateral boundary condition for multi-level prediction models. *Quart. J. Roy. Meteor. Soc.*, **102**, 405-418.
- Deardorff, J.W., 1977: A parameterization of ground surface moisture content for use in atmospheric prediction models. *J. Appl. Meteor.*, **16**, 1182-1185.
- Jackson, R.D., 1973: Diurnal changes in soil water content during drying. *Field Soil Water Regime*, Soil Sci. Soc. Amer., 37-55.
- Katayama, A., 1972: A simplified scheme for computing radiative transfer in the troposphere. *Tech. Rep. No. 6*, Dept. of Meteor., UCLA. 77 pp.
- Mellor, G.L. and A.F. Blumberg, 1985: Modeling vertical and horizontal diffusivities with the sigma coordinate system. *Mon. Wea. Rev.*, **113**, 1379-1383.
- Muench, H.S., 1983: Experiments in objective aviation weather forecasting using upper-level steering. *AFGL-TR-83-0328*, 44pp. ADA143393.
- Muench, H.S., 1988: Compositing local area forecast techniques. *AFGL-TR-88-0216*, 33 pp. ADA210802.
- Muench, H.S., and D.A. Chisholm, 1985: Aviation weather forecasts based on advection: Experiments using modified initial conditions and improved analyses. *AFGL-TR-85-0011*, 57 pp. ADA160369.
- Nickerson, E.C., 1979: On the simulation of airflow and clouds over mountainous terrain. *Beit. Atmos. Phys.*, **52**, 161-177.
- Nickerson, E.C., E. Richard, R. Rosset, and D.R. Smith, 1986: The numerical simulation of clouds, rain, and airflow over the Vosges and Black Forest mountains: A meso- β model with parameterized microphysics. *Mon. Wea. Rev.*, **114**, 398-414.
- Peilke, R.A., 1984: *Mesoscale Meteorological Modeling*, Academic Press, 612 pp.

- Perkey D. J., and C.W. Kreitzberg, 1976: A time-dependent lateral boundary scheme for limited-area primitive equation models. *Mon. Wea. Rev.*, **104**, 744-755.
- Seitter, K.L., 1987: The specification of lateral boundary conditions in three-dimensional mesoscale numerical models. Final Report. *AFGL-TR-87-0015*, 129 pp. ADA179185.
- Wetzel, P.J., 1978: A detailed parameterization of the atmospheric boundary layer. *Atmos. Sci. Paper* 302, Colorado State University.
- Yamada, T., 1979: Prediction of the nocturnal surface inversion height. *J. Appl. Meteor.*, **18**, 526-531.
- Zeman, O., and H. Tennekes, 1977: Parameterization of the turbulent energy budget at the top of the daytime atmospheric boundary layer. *J. Atmos. Sci.*, **34**, 111-123.
- Zhang, D.-L., H.-R. Chang, N.L. Seaman, T.T. Warner, and J.M. Fritsch, 1986: A two-way interactive nesting procedure with variable terrain resolution. *Mon Wea. Rev.*, **114**, 1330-1339.